Power flow and structural intensity analyses of Acoustic Black Hole beams

Yuhang Wang [a], Jingtao Du [a,*], Li Cheng [b,*]

[a] College of Power and Energy Engineering, Harbin Engineering University, Harbin 150001, PR China
[b] Department of Mechanical Engineering, The Hong Kong Polytechnic University, Hong Kong 999077, PR China

ARTICLE INFO

ABSTRACT

A truthful description of the energy transport process is vital for the understanding of the Acoustic Black Hole (ABH) effect and its applications. One of the parameters, which can depict such a physical process is the power flow, whose calculation involves higher-order derivatives of the structural displacement function. This however requires an accurate and sufficiently smooth fitting of the structural responses which can hardly be achieved by the existing semi-analytical models on ABH structures. To tackle the problem, an energy formulation, in conjunction with a Rayleigh-Ritz procedure, is proposed for an ABH beam, whose thickness variation is described as a general Fourier expansion. The transverse displacement of the beam is constructed using Fourier series with supplementary auxiliary functions. This treatment ensures the continuity and the smoothness of all relevant derivatives terms in the entire calculation domain, thus allowing the calculation of the power flow and structural intensity. Numerical examples are presented to illustrate the reliability and the effectiveness of the established model. Numerical analyses on power flow and structural intensity show the spatial and frequency characteristics of the energy transmission process and reveal the ABH-specific mechanisms. While providing an efficient analysis tool, this work enriches the existing understanding on the dynamic behavior of ABH structures.

© 2019 Published by Elsevier Ltd.

1. Introduction

The Acoustic Black Hole (ABH) phenomenon, featuring a gradual phase velocity reduction of the flexural waves in a thin-walled structure with a power-law tailored decreasing thickness, has been explored for various applications such as vibration and noise control [1–3], energy harvesting [4,5] and wave manipulations [6,7]. Thanks to the ABH-specific wave retarding and energy focalization feature, significant vibration attenuation can be achieved by using a small amount of damping near the tip of the ABH taper. Meanwhile, the creation of subsonic waves (acoustically slow structural waves) reduces the sound radiation efficiency of the structure, also conducive to noise reduction. Since the pioneer work of Mironov [8] and a series of significant work of Krylov et al. [9–12], interest in exploring various aspects of ABH effects has experienced a flourishing development during the past twenty years. Typical work ranges from theoretical to experimental studies as well as various applications using both ABH beams [13–15] and plane structures of various shapes such as circular [16,17], elliptical [18,19] and rectangular plates [20].

---

* Corresponding authors.
  E-mail addresses: dujingtao@hrbeu.edu.cn (J. Du), li.cheng@polyu.edu.hk (L. Cheng).

The realization of the effective ABH effect and its successful application require a thorough understanding of the wave propagation process and a meticulous handling of various structural parameters. This requires a truthful description and the modelling of energy transport process. Efforts have been made using different metrics such as reflection coefficient [21], cross-point mobility [15,22,23] and energy distribution [24,25] etc. Although these works allow the quantification of the ABH effect from different angles, they mainly focus on the end result of the ABH effect instead of the wave propagation process itself. As a useful attempt, experimental approach was adopted to visualize the wave propagation using a combined laser excitation technique and laser scanning vibrometer measurement [24].

A predictive model, capable of characterizing the energy transport process in ABH structure, is of great interest to guide the practical design of ABH structures. One of the physical parameters which are able to inform the energy propagation process is the structural power flow, or the structural intensity. Power flow is a physical quantity that synthetically considers the vibratory velocity and internal force in a structure and gives information on the input power, dominant transmission paths as well as energy dissipation within the structure. Through decades of development, power flow analysis has been applied to study many types of complex structures, both numerically and experimentally [26–35]. As far as ABH structures are concerned, only numerical simulations using Finite Element Analysis have been attempted so far [25,36].

Apart from the widely used FEM/BEM methods, effort has also been made in developing semi-analytical modeling techniques for beams [15] and plates [37] based on different types of wavelets [15,22]. Although these works show the advantages of the semi-analytical modeling and its accuracy in predicting the structural response, these models cannot provide the accuracy needed for the higher order differential calculation of displacement functions which is required for the calculation of internal forces for power flow or structural intensity determination.

Motivated by this, a revamped semi-analytical modeling approach is proposed in this paper for the power flow analysis of an elastically restrained ABH beam, whose thickness profile is expressed in a general form via Fourier series. An energy formulation in conjunction with Rayleigh-Ritz procedure is employed for the dynamic description of the ABH beams, in which the standard Fourier series, supplemented by the boundary smoothened auxiliary terms, is constructed as the admissible function for the structural displacement decomposition. This treatment is demonstrated to ensure the continuity and the smoothness of the displacement function of the system so that all the relevant spatial derivatives of various order required for the calculation of internal forces in the power flow calculation can be obtained straightforwardly through the standard term-by-term differential operation. Numerical examples are then presented to validate the correctness and the effectiveness of the proposed model through comparisons with results from other approaches. Using the proposed model, power flow and structural intensity in ABH beam are investigated to show the energy flow across the structure and its dissipation in spatial domain in relation to the damping layers. Finally, conclusions are given.

2. Theoretical formulation

2.1. Elastically restrained beams with arbitrary thickness variation

As illustrated in Fig. 1, we consider a general Euler-Bernoulli beam undergoing transverse vibration under a concentrated force excitation F at x_f, with the coordinate origin being located at the left end of the beam. The whole system is assumed to be symmetrical with respect to the mid-line of the beam. The beam, having a length L and a constant width b, has an
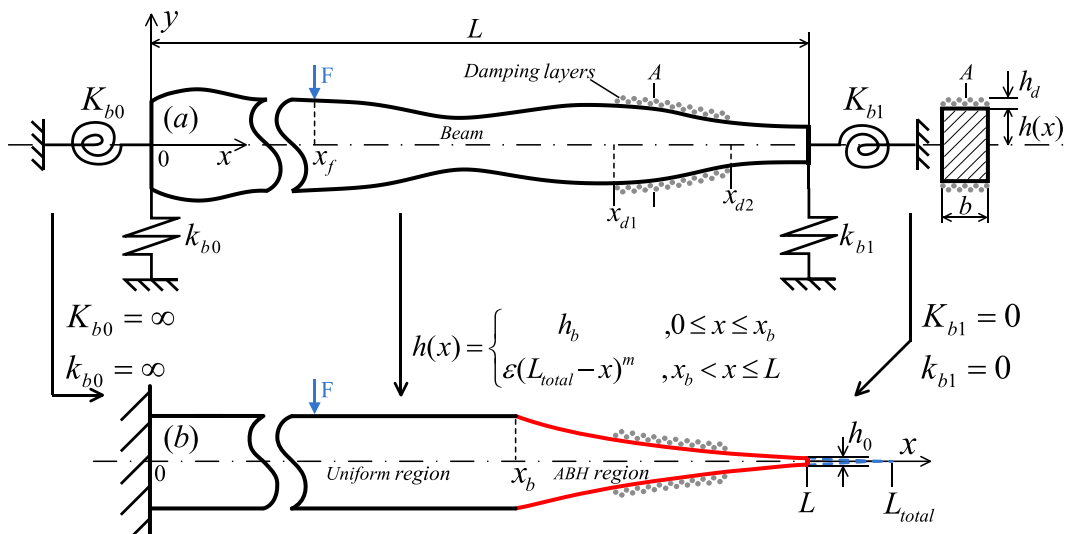

Fig. 1. A model of elastically retrained beam with arbitrary thickness variation and fully coupled damping layers.

arbitrary thickness profile $h(x)$ and is symmetrically covered by a damping layer of thickness h_d. Boundary conditions of the beam are simulated by introducing a set of elastic springs at both ends against translation and rotation, respectively. For example, k_{b0} and K_{b0} denote the translational and rotational spring stiffness at the end $x = 0$. Through a proper assignment of the restraining spring coefficients, all the classical boundary conditions as well as their combinations can be readily simulated. Structural damping is simulated through a complex Young's modulus $E = E(1 + j\eta)$, with η being the damping loss factor, taking different values for the beam and the damping layer.

The existing description of the ABH profile in the literature is mainly confined to a power-law form, thus limiting the tuning of the ABH design to the adjustment of the power-law index and its coefficients. To envisage a more general thickness profile, which may eventually expand the design space of the ABH structure, a general thickness distribution function $h(x)$ is considered and transformed into Fourier series. The corresponding cross-section area $S^{beam}(x) = 2bh(x)$ and the moment of inertia $I^{beam}(x) = 2bh^3(x)/3$ write, respectively

$$S^{beam}(x) = \sum_{n=0}^{\infty} \alpha_n^{beam} \cos \lambda_{Ln} x, \tag{1}$$

$$\alpha_n^{beam} = \begin{cases} \frac{2}{L} \int_0^L S^{beam}(x) dx, n = 0 \\ \frac{2}{L} \int_0^L S^{beam}(x) \cos(\lambda_{Ln} x) dx, n \neq 0 \end{cases}, \tag{2}$$

$$I^{beam}(x) = \sum_{n=0}^{\infty} \beta_n^{beam} \cos \lambda_{Ln} x, \tag{3}$$

and

$$\beta_n^{beam} = \begin{cases} \frac{2}{L} \int_0^L I^{beam}(x) dx, n = 0 \\ \frac{2}{L} \int_0^L I^{beam}(x) \cos(\lambda_{Ln} x) dx, n \neq 0 \end{cases}. \tag{4}$$

For the damping layer, which is considered in a fully coupled manner, $S^{damp}(x) = 2bh_d$ and $I^{damp}(x) = 2b[3 h^2(x)h_d + 3 h(x) h_d^2 + h_d^3]/3$. They are also transformed into Fourier series, similar process is followed and the corresponding coefficients are expressed as $\alpha_n^{beam/damp}$ and $\beta_n^{beam/damp}$. In this way, all the thickness variation information can be covered and stored in its Fourier series coefficients. The potential benefits can be understood from two aspects. The first is that all the subsequent spatial integration will be performed for these Fourier cosine series. The calculation can be analytically conducted, thus ensuring a much higher calculation accuracy and efficiency. Secondly, further optimization of the thickness profile can be implemented by easily adjusting these Fourier coefficients $\alpha_n^{beam/damp}$ and $\beta_n^{beam/damp}$, accordingly.

The above described beam with a general thickness profile retreats to an ABH beam by setting the thickness variation $h(x)$ as a power-law function in the right part of the beam as illustrated in Fig. 1 (bottom plot). The thickness variation function across the entire ABH beam (including a uniform part and ABH part) is expressed as:

$$h(x) = \begin{cases} h_b & , 0 \leq x \leq x_b \\ \varepsilon(L_{total} - x)^m & , x_b < x \leq L \end{cases} \tag{5}$$

As shown in Fig. 1, other geometrical parameters, such as the total length L_{total} and the inevitable thickness truncation resulting from the practical manufacturing limitation, h_0, should satisfy the following relationship:

$$\begin{cases} L_{total} = (h_b/\varepsilon)^{1/m} + x_b \\ h_0 = 2\varepsilon(L_{total} - L)^m \end{cases} \tag{6}$$

The ABH profile described in Eq. (5) can be converted into Fourier space by using the profile information transformation Eqs. (1)–(4). By substituting the obtained Fourier series coefficients into the original dynamic model established above, vibration analyses on the ABH beam with the specified thickness profile can be performed.

2.2. Fully coupled dynamic modeling of the beam structure

A fully coupled dynamic model is established based on the Euler-Bernoulli beam theory and energy principle. The system Lagrangian L_s can be written as

$$L_s = V - T - W \tag{7}$$

where V and T are the total potential and kinetic energies, including the elastic boundary restraints as well as the damping layers. W is the work done by the concentrated force applied at the beam structure.

The potential energy V writes

$$V = \frac{E^{beam}}{2} \int_0^L I^{beam}(x) \left(\frac{\partial^2 w(x)}{\partial x^2} \right)^2 dx + \frac{E^{damp}}{2} \int_{x_{d1}}^{x_{d2}} I^{damp}(x) \left(\frac{\partial^2 w(x)}{\partial x^2} \right)^2 dx + \frac{1}{2} K_{b0} \left(\frac{\partial w(x)}{\partial x} \right)^2 \bigg|_{x=0} + \frac{1}{2} k_{b0} w(x)^2 \bigg|_{x=0}$$

$$+ \frac{1}{2} K_{b1} \left(\frac{\partial w(x)}{\partial x} \right)^2 \bigg|_{x=L} + \frac{1}{2} k_{b1} w(x)^2 \bigg|_{x=L} \tag{8}$$

in which the two terms in the first row are related to the strain potential energies due to the deformation of the host ABH beam and that of the damping layers, respectively. Here, damping layers are assumed to be fully coupled with the host beam over its coated region $[x_{d1}, x_{d2}]$. The remaining four terms in the second row represent the elastic potential energies stored in the rotational and translational springs at both ends.

The kinetic energy T can be written as

$$T = \frac{1}{2} \rho^{beam} \omega^2 \int_0^L S^{beam}(x) w(x)^2 dx + \frac{1}{2} \rho^{damp} \omega^2 \int_{x_{d1}}^{x_{d2}} S^{damp}(x) w(x)^2 dx \tag{9}$$

The work W done by the external point force excitation is

$$W = \int_0^L F \delta(x - x_f) w(x_f) dx \tag{10}$$

where F denotes the external force and $\delta(x)$ is the Dirac delta function.

2.3. Improved Fourier series solution of the beam structure

The discretization of the above formulation requires the construction of a set of admissible functions with sufficiently smooth properties. Fourier series is usually employed for the displacement expansion in dynamic the modeling of beam structure as

$$w(x) = \sum_{m=0}^{\infty} C_m \cos(\lambda_{Lm} x) \tag{11}$$

in which, C_m is the unknown Fourier expansion coefficient and $\lambda_{Lm} = m\pi/L$, and the corresponding first and third order derivatives at the end $x = 0$ write

$$\frac{\partial w(x)}{\partial x} \bigg|_{x=0} = -\sum_{m=0}^{\infty} C_m \lambda_{Lm} \sin(\lambda_{Lm} 0) = 0 \tag{12}$$

$$\frac{\partial^3 w(x)}{\partial x^3} \bigg|_{x=0} = \sum_{m=0}^{\infty} C_m \lambda_{Lm}^3 \sin(\lambda_{Lm} 0) = 0 \tag{13}$$

Similar results can be obtained on the other end of the beam $x = L$. It can be seen that the first and third order derivatives with respect to the spatial coordinate at both ends are systematically zero. However, for the general elastic boundary restraints considered in this work, the non-zero spatial differentials of these orders will be required to represent the following force equilibrium and geometric coordination relationship; namely, taking the end $x = 0$ as an example,

$$k_{b0} w|_{x=0} = -EI(x) \frac{\partial^3 w}{\partial x^3} \bigg|_{x=0}, \tag{14}$$

$$K_{b0} \frac{\partial w}{\partial x} \bigg|_{x=0} = EI(x) \frac{\partial^2 w}{\partial x^2} \bigg|_{x=0} \tag{15}$$

Submitting Eq. (11) into Eqs. (12) and (13), clearly shows that the standard Fourier cosine or sine series cannot satisfy such elastic boundary conditions due to its differential discontinuities of various order spatial derivatives at the boundaries. To satisfy the differential continuity requirements by the force equilibrium and geometric coordination at the general elastic end supports [38–40], the standard Fourier series is supplemented by boundary smoothened auxiliary functions as follows:

$$w(x) = \sum_{m=0}^{\infty} C_m \cos(\lambda_{Lm} x) + a \zeta_1(x) + b \zeta_2(x) + c \zeta_3(x) + d \zeta_4(x) \tag{16}$$

in which $\zeta_1(x)$, $\zeta_2(x)$, $\zeta_3(x)$ and $\zeta_4(x)$ are four auxiliary functions, weighted by four coefficients a, b, c and d, respectively.

The main purpose of introducing auxiliary functions is to remove the boundary discontinuities of the first and third order spatial derivatives associated with the original Fourier series, as shown in Eqs. (12) and (13). The construction of these

supplementary functions is not unique mathematically, while appropriate choice of their forms will simplify the subsequent mathematical operations. With this in mind, they are chosen as:

$$\zeta_1(x) = \frac{9L}{4\pi}\sin\left(\frac{\pi x}{2L}\right) - \frac{L}{12\pi}\sin\left(\frac{3\pi x}{2L}\right),$$ (17)

$$\zeta_2(x) = -\frac{9L}{4\pi}\cos\left(\frac{\pi x}{2L}\right) - \frac{L}{12\pi}\cos\left(\frac{3\pi x}{2L}\right)$$ (18)

$$\zeta_3(x) = \frac{L^3}{\pi^3}\sin\left(\frac{\pi x}{2L}\right) - \frac{L^3}{3\pi^3}\sin\left(\frac{3\pi x}{2L}\right),$$ (19)

and

$$\zeta_4(x) = -\frac{L^3}{\pi^3}\cos\left(\frac{\pi x}{2L}\right) - \frac{L^3}{3\pi^3}\cos\left(\frac{3\pi x}{2L}\right).$$ (20)

In each supplementary function above, the choice of trigonometric function and their combination are made based on the criteria of removing the first and third differential discontinuities encountered in the general elastic boundary conditions Eqs. (14) and (15). The corresponding weighting coefficients are assumed to realize the normalization condition for the subsequent functional value as well as their spatial derivatives at both ends of the beam. It is easy to verify that

$$\begin{bmatrix} \zeta_1'(0) & \zeta_2'(0) & \zeta_3'(0) & \zeta_4'(0) \\ \zeta_1'(L) & \zeta_2'(L) & \zeta_3'(L) & \zeta_4'(L) \\ \zeta_1'''(0) & \zeta_2'''(0) & \zeta_3'''(0) & \zeta_4'''(0) \\ \zeta_1'''(L) & \zeta_2'''(L) & \zeta_3'''(L) & \zeta_4'''(L) \end{bmatrix} = \begin{bmatrix} 1 & 0 & 0 & 0 \\ 0 & 1 & 0 & 0 \\ 0 & 0 & 1 & 0 \\ 0 & 0 & 0 & 1 \end{bmatrix}$$ (21)

To better demonstrate the first and third order differential properties of these supplementary functions, their corresponding functional graphs are calculated and presented in Fig. 2. It can be seen that these supplementary function terms can effectively remove the differential discontinuities of the original Fourier series Eqs. (11)–(13). Then, the improved Fourier series expansion of ABH flexural displacement Eq. (16) will be sufficiently smooth in the whole solving range, including both general elastic ends, which is vital to improve the series solution convergence and accuracy. More importantly, all the spatial derivatives of various order needed for the power flow and structural intensity calculation can then be derived in any field point of ABH beam structure, as to be demonstrated later.

Substituting Eq. (16) into the system Lagrangian Eqs. (7)–(10), in conjunction with Rayleigh-Ritz procedure, the discretized system equation can be derived and expressed in the following matrix form:

$$(\boldsymbol{K} - \omega^2 \boldsymbol{M})\boldsymbol{R} = \boldsymbol{F}$$ (22)

where $\boldsymbol{M}$ and $\boldsymbol{K}$ are the mass and stiffness matrices, respectively; ω is the angular frequency; $\boldsymbol{R}$ and $\boldsymbol{F}$ are the coefficient vectors of the improved Fourier series expansion and the external force loading, respectively. Eq. (22) can be solved through standard matrix inversion operation. By removing the force vector on the right-hand side, all the modal information can be obtained by solving a standard eigen-value problem. Substitution of the corresponding eigenvectors into the improved Fourier series displacement expression, one can get the mode shapes of the ABH beam structure.
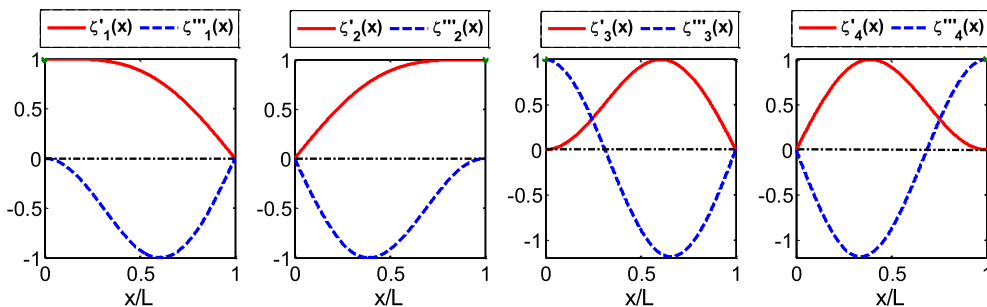

Fig. 2. Graphs of the first and third order derivatives for these four auxiliary functions.

2.4. Power flow and structural intensity of ABH beam

Thanks to the derivative continuity characteristics of the constructed displacement expression, all the internal forces required for the structural intensity calculation can be determined in a straightforward way through a term-by-term differential operation. The time-averaged input power flow P_{input} is defined as

$$P_{input} = \frac{1}{T_P} \text{Re} \left\{ \int_0^{T_p} F(t) v(t) \mathrm{d}t \right\} \tag{23}$$

where $v(t)$ is the transverse velocity at the force application position; t and T_p are the time and observation period, respectively. For a harmonic excitation, with $F(t) = Fe^{j\omega t}$ and $v(t) = ve^{j\omega t}$, Eq. (23) becomes

$$P_{input}(\omega) = \frac{1}{2} \text{Re} \{ F^* v \} = \frac{1}{2} \text{Re} \{ Fv^* \} \tag{24}$$

where * denotes the complex conjugate and $\text{Re}\{\}$ the real part of the complex variable. Using the driving point mobility, namely $v = YF$, Eq. (24) can be rewritten as

$$P_{input}(\omega) = \frac{1}{2} \text{Re} \{ F^* Y(\omega) F \} = \frac{1}{2} |F|^2 \text{Re} \{ Y(\omega) \} \tag{25}$$

As to the vibration energy transmission in the beam structure, the structural intensity $I_{x,transfer}$, defined as the power flow through per unit cross sectional area of the beam, is expressed as

$$I_{x,transfer}(x) = \frac{1}{2} \text{Re} \left\{ Q_x \left(\frac{\partial w}{\partial x} \right)^* - M_x \left(\frac{\partial^2 w}{\partial x \partial t} \right)^* \right\} \tag{26}$$

in which Q_x and M_x are the transverse shear force and bending moment, respectively. These two quantities can be calculated through the higher order spatial derivatives of beam displacement function, namely

$$M_x = EI(x) \frac{\partial^2 w}{\partial x^2} \tag{27}$$

$$Q_x = E \frac{\partial}{\partial x} \left[I(x) \frac{\partial^2 w}{\partial x^2} \right] \tag{28}$$

As mentioned before, the supposition of the standard Fourier series and auxiliary functions Eqs. (17)–(20) can guarantee sufficiently continuous and spatially smooth derivatives of various order in the entire solving domain, including the general elastic end supports. Making use of the dynamic response information **R** obtained from Eq. (22), the power flow and structural intensity can be derived through a straightforward post-processing operation.

3. Numerical results and discussions

In this section, numerical examples are presented to demonstrate the correctness and the effectiveness of the proposed model. With the model, power flow and structural intensity of ABH beams with or without damping layers are investigated in details.

3.1. Model validation

To check and demonstrate the ability of the current model in reaching the high frequency range, a uniform simply-supported beam is first chosen for the comparative study, due to the existence of the exact solutions. Simulation parameters used are given in Table 1.

In the current model, the uniform beam can be obtained by setting the thickness profile function $h(x)$ as a constant. Simply-supported boundary condition is realized by setting the spring stiffness into zero or infinity, accordingly. Plotted in Fig. 3 is the comparison between the modal parameters calculated from the current model and the analytical results, in which the first 1000 modes are considered. Fig. 3(a) shows a nice agreement between the two sets of results. Quantita-

Table 1
Parameters for the simply supported uniform beam.

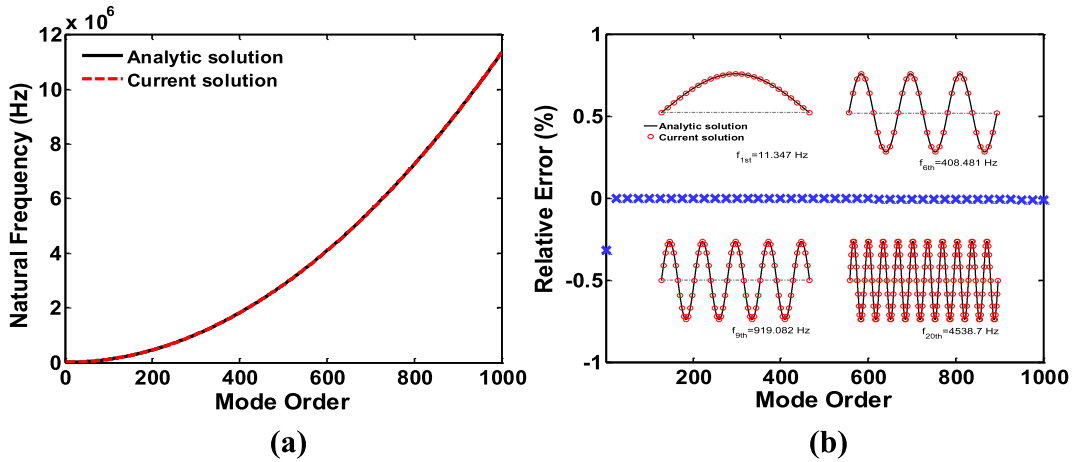| Geometrical parameters	Material parameters
$L = 0.72$ m	$E = 210$ GPa
$h(x) = 0.00125$ m	$\eta = 0.005$
$b = 0.01$ m	$\rho = 7800$ kg/m^3

Fig. 3. Comparison of modal parameters of a uniform beam from exact and current solutions (a) natural frequencies; (b) relative error with representative mode shapes.

tively, the relative error in terms of natural frequencies and representative mode shapes are given in Fig. 3(b). Overall speaking, the accuracy of the model and its ability in reaching very high-order modes are deemed satisfactory.

To demonstrate the properties of the series expansion Eq. (16), various truncation terms are chosen for the calculation of the frequency response curve of the beam displacement and the shear force, respectively. In the numerical simulations, a unit point force is applied on the beam at $x_f = 0.15$ m, and the observing response point is at $x = 0.65$ m. Shown in Fig. 4 is the acceleration curves computed using various truncation terms, alongside the results from the analytic solution. It can be observed that the current model rapidly converges to the analytic solution with the increase of the truncated number M, whose value is to be determined depending on the frequency to be reached.

The calculation of structural intensity requires the higher order spatial differentials. It is therefore surmised that more terms in the truncated series would be required to obtain an accurate evaluation of the internal forces. To demonstrate this, the shear force at $x = 0.65$ m is calculated using different truncation terms, as shown in Fig. 5. Comparing with Fig. 4, it can be found that, for the internal shear force calculation, tiny difference with the analytic solution exists at those frequencies corresponding to the system resonant resonances. With the further increase of the truncated number to $M = 50$, this difference reduces to a trivial level, as compared with the analytic solution.

Let us now focus on the ABH beam structure. For comparisons, the cantilever ABH beam previously used in Tang et al. [15] is used, with parameters listed in Table 2. In the present model, the ABH beam can be obtained by substituting the Fourier expansion coefficients of the ABH thickness variation profile into the solution framework. In this work, the overall profile of the beam, including both the uniform part and ABH region, is expanded into Fourier series as a whole. In the present case, 1980 terms are used in the series to achieve a sufficiently accurate description of the ABH beam. The cantilever conditions can be achieved by setting the spring restraining stiffness into infinity on $x = 0$, and those into zero on $x = L$, respectively.
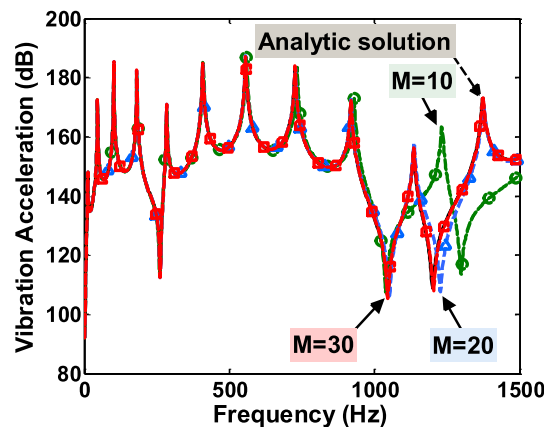

Fig. 4. Convergence of vibration acceleration frequency response at $x = 0.65$ m under various truncation numbers.
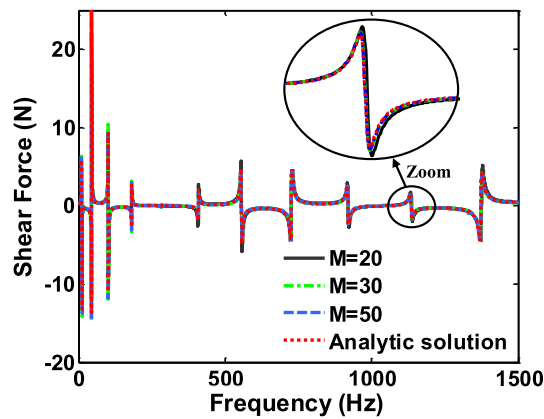
Fig. 5. Frequency response of internal shear force at $x = 0.65$ m predicted using various truncated numbers.

Table 2
Simulation model parameters of a cantilever ABH beam.

Geometrical parameters	Material parameters
$\varepsilon = 0.5$ m^{-1}	$E_b = 210$ Gpa
$m = 2$	$\rho_b = 7800$ kg/m^3
$h_b = 0.00125$ m	$\eta_b = 0.005$
$x_b = 0.05$ m	$E_d = 5$Gpa
$L = 0.09$ m	$\rho_d = 950$ kg/m^3
$L_{total} = 0.1$ m	$\eta_d = 0.3$
$h_0 = 0.0001$ m	

Tabulated in Table 3 is the comparison of the first forty modal frequencies of the ABH beam obtained from the current model and a Finite Element model in COMSOL Multiphysics. In the FEM calculation using COMSOL, Euler-Bernoulli beam elements are used with a mesh size of typically 9×10^{-5} m. Further decrease of mesh size would not generate noticeable variations in the predicted results. The current model uses $M = 180$ due to the increasing complexity of the ABH taper. The comparison in Table 3 shows that the current model can give very accurate prediction of the modal parameters as compared with those from FEM, even at very higher frequencies.

The forced vibration, with a unit point force applied at $x = 0.02$ m, is investigated. Presented in Fig. 6 is a comparison of the acceleration response of the ABH beam at $x = 0.075$ m, calculated from the current model and the FEM, respectively. Two representative mode shapes, namely the fifth and twentieth modes, are also given in the figure. It can be observed that both

Table 3
Comparison of natural frequencies of ABH beam calculated from current model and FEM.

| Mode order	Current (Hz)	FEM (Hz)	Error (%)	Mode order	Current (Hz)	FEM (Hz)	Error (%)
1	433.22	432.91	0.0716	21	146267.3	146,270	−0.0018
2	1664.1	1669.5	−0.3235	22	160688.1	160,690	−0.0012
3	2981.4	2972.8	0.2893	23	175984.7	175,980	0.0027
4	5071.7	5071.8	−0.0020	24	191841.5	191,840	0.0008
5	8000.7	8000.8	−0.0012	25	208401.6	208,390	0.0056
6	11338.8	11,339	−0.0018	26	225766.4	225,760	0.0028
7	15563.9	15,564	−0.0006	27	243645.0	243,630	0.0062
8	20446.1	20,446	0.0005	28	262368.2	262,350	0.0069
9	25878.0	25,878	0.0000	29	281736.3	281,710	0.0093
10	32219.3	32,219	−0.0009	30	301718.2	301,680	0.0127
11	39069.7	39,070	−0.0008	31	322559.4	322,510	0.0153
12	46660.8	46,661	−0.0004	32	343930.2	343,860	0.0204
13	55041.9	55,042	−0.0002	33	366077.6	365,990	0.0239
14	63921.0	63,921	0.0000	34	388967.2	388,850	0.0301
15	73673.5	73,694	−0.0278	35	412407.9	412,250	0.0383
16	84038.0	84,038	0.0000	36	436723.4	436,520	0.0466
17	95030.7	95,031	−0.0003	37	461629.1	461,370	0.0562
18	106882.5	106,880	0.0023	38	487235.2	486,900	0.0688
19	119239.9	119,240	−0.0001	39	513669.5	513,250	0.0817
20	132395.6	132,400	−0.0033	40	540644.5	540,120	0.0971
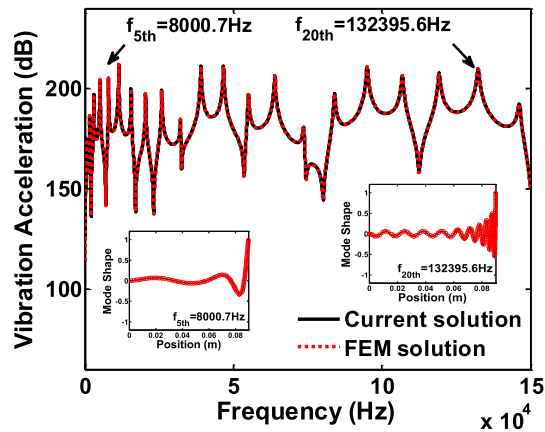
Fig. 6. Comparison of vibration acceleration response of ABH beam calculated from the current model and FEM in COMSOL.
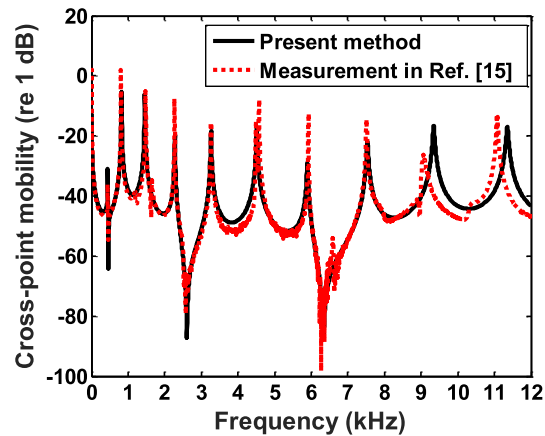

Fig. 7. Comparison of a representative cross-point mobility of ABH beam between the current prediction and experimental measurement made in Ref. [15].

the trend and the magnitude of vibration frequency response, as well as the two arbitrarily selected mode shapes, agree very well with each other between these two approaches in the whole frequency range of interest. Various resonant peaks in the frequency response curve actually correspond to the structural modes of the ABH beam. When frequency increases, the expected ABH effect exhibits more clearly in terms of wave compression and amplitude increase towards the tip of the beam.

In order to validate the current model, experimental results by Tang et al. [15] are used for comparison. The configuration is the same as detailed in Ref. [15], including all geometrical and material parameters of the ABH beam, as well as the test-rig. Comparisons in terms of the cross-point mobility of the ABH beam, with an excitation force applied to the uniform beam part and response measured inside the ABH region, are presented in Fig. 7.

Fig. 7 shows that the predicted results from the current model agree well with the experimental data within a large frequency range, roughly up to 9 kHz. Discrepancies between the two sets of results start to appear after, since the current model is based on Euler-Bernoulli theory, in which the shear and rotational effects are neglected. These effects, however, show increasing influences at extremely high frequencies. Nevertheless, the proposed model is deemed good enough to characterize the dynamic behavior of the ABH beam in a satisfactory manner.

3.2. Power flow and structural intensity of an ABH beam without damping layers

The total input power can be estimated from the applied force amplitude and the point mobility at the excitation position $x_f = 0.02$ m. Two representative observing points are also chosen for the computation of transfer power flow, for which one ($x_m = 0.04$ m) is located in the uniform region of the beam, whilst the other ($x_m = 0.07$ m) in the ABH region. Fig. 8 presents the variation of the total input power and power flow at the two observing points. It can be observed that, dominated by the resonant peaks of the structure, the transfer power flow is systematically smaller than the input component. In the entire frequency range, due to the energy separation at the excitation point and the dissipation caused by the structural damping,
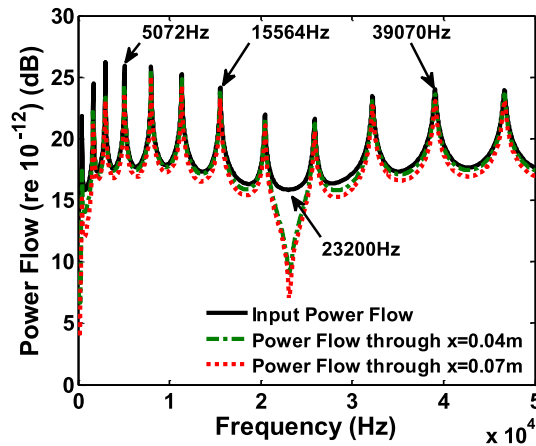
Fig. 8. Frequency response of the total input and transfer power flow in ABH beam structure.

the further away from the excitation source is, the lower the transfer power flow across that location is. At certain excitation frequency, *e.g.* 23200 Hz, the transfer power flow decreases significantly. This observation is consistent with that made in [41] when a loss of the ABH was observed. From the viewpoint of power flow, it is clear that there is little energy transfer across that location at such a frequency, and the vibration energy mainly concentrates within the uniform part of the ABH beam delimited by the left-side beam boundary and the excitation point.

In order to better understand the energy transport process and its underlying mechanism associated with the ABH effect, the structural intensity distribution across the entire beam is examined for some representative modal frequencies, namely $f_4 = 5072$ Hz, $f_7 = 15564$ Hz and $f_{11} = 39070$ Hz, as shown in Fig. 9. In the sub-plots, the positive and negative values of the structural intensity denote the power flow to the right- and left-hand side directions across each field point, respectively. The structural intensity values at each side of excitation point therefore carry opposite signs, leading to an abrupt change at the forcing location. To eliminate the effect of the total input power amplitude, which is frequency dependent, the normalized structural intensity is utilized, by normalizing the structural intensity to the total input power. In Fig. 9(a), the excitation position clearly separates two different zones with positive and negative intensity values, in accordance with two opposite energy flow directions. It is clear that the energy flows into the structure from the excitation position and spreads over to both sides of the beam, and the structural intensity gradually approaches to zero at the two ends. Compared with the left part, the vibrational power mainly flows to the right part into the ABH region. With the increase of the distance from the excitation position, there is a decreasing trend for the structural intensity, along with an oscillation of the decreasing speed during this process. Note the spatial gradient of the structural intensity, namely the divergence, actually represents the strength of the energy dissipation. Therefore, the afore-observed changes indicate that energy is dissipated along the beam, which is accentuated when approaching the ABH tip. With the increase of frequency, at 15564 Hz and 39070 Hz, a relatively uniform gradient of structural intensity distribution can be observed (Fig. 9(b) and (c)). This suggests that the vibrational energy is dissipated more uniformly along the beam structure due to its structural damping at high frequencies. Note that in the above simulations, only internal structural damping is included without any damping layer. In a sense, although the energy focalization is achieved, dissipation at the tip of the beam is still not enough. Therefore, the totality of the ABH effect cannot be materialized in the present scenario.

Based on the definition of flexural structural intensity in beam Eq. (26), the two constituent components, corresponding to the shear force and the bending moment respectively, are involved in the structural intensity at each field point. To gain in-depth insights, these two parts are separately calculated with results plotted in Fig. 10, for the same frequencies used in Fig. 9(a) and (c). It can be observed that these two components exhibit a similar trend with the total structural intensity. At relatively low frequency, shown in Fig. 10(a), an oscillation and alternation between these two components can be observed especially on the right side of the excitation point. When the excitation frequency gets much higher, as illustrated in Fig. 10 (b), both components almost coincide with each other in the right region starting from a certain distance apart from the excitation force. This is analogous to the well-known behavior of an infinite beam in the high frequency range. The fact that it happens more clearly at a high frequency (39070 Hz) indicates that the ABH tip behaves more like an anechoic termination when frequency is high enough.

It is also relevant to re-examine the phenomenon of the loss of the ABH effect discussed before at 23200 Hz from the power flow viewpoint. To this end, the corresponding normalized structural intensity distribution and displacement response are given in Fig. 11. It can be seen that the totality of the vibration energy almost goes to the left part the beam from the excitation position. The corresponding displacement response curve (Fig. 11(b)) also confirms the strong energy localization phenomenon.
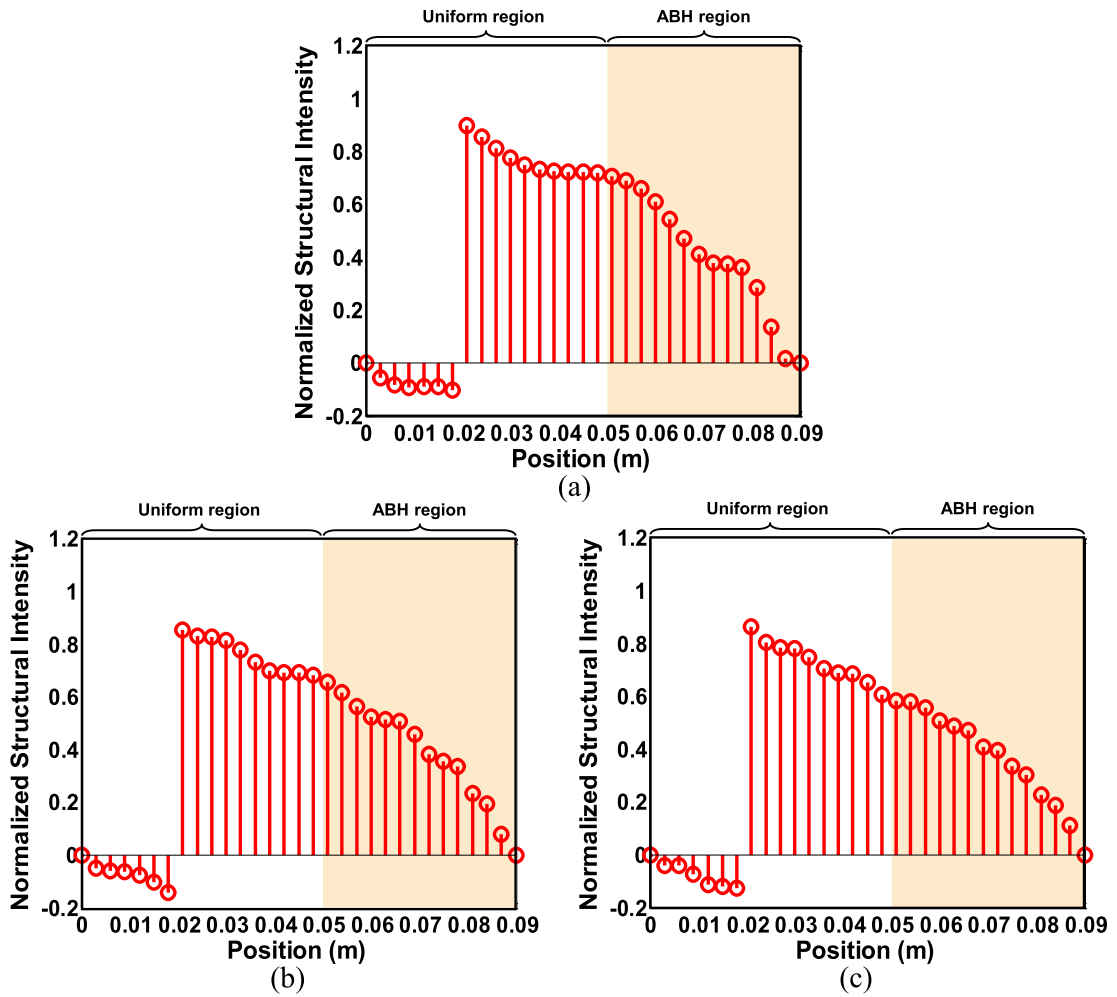
Fig. 9. Normalized structural intensity distribution in ABH beam under resonant excitation frequencies: (a) 5072 Hz; (b) 15564 Hz; (c) 39070 Hz.
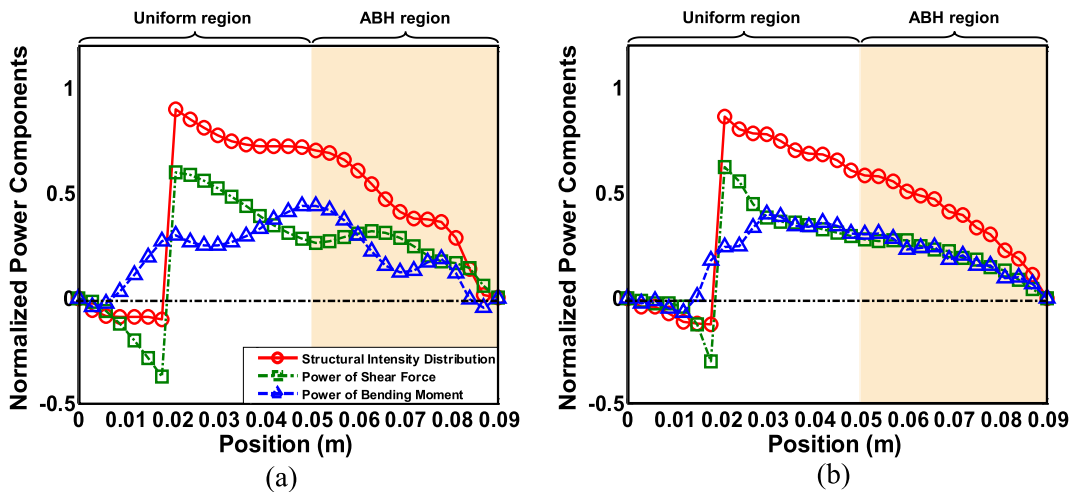

Fig. 10. Normalized power components due to the shear force and bending moment at two representative frequencies: (a) 5072 Hz; (b) 39070 Hz.
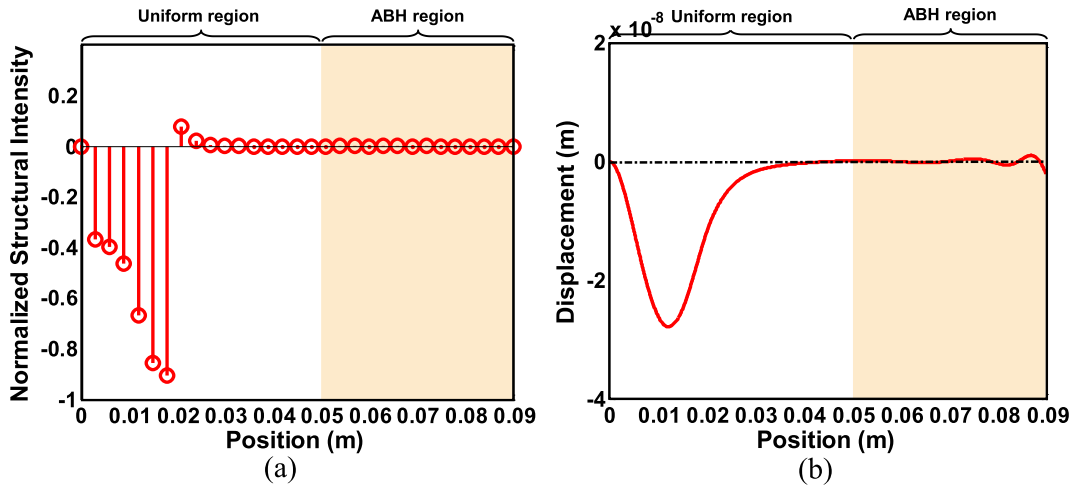
Fig. 11. Distribution of structural intensity and vibration displacement across the beam at ABH-failed frequency: (a) structural intensity; (b) vibration displacement.

3.3. Energy transmission in an ABH beam with damping layers

In principle, complete ABH effect takes place only with the use of the damping layers due to the existence of the truncated thickness at the end of the taper. With this in mind, the same beam as the one used above but with additional damping layers is investigated. The same group of parameters as those presented in Table 2 is used. Damping layers (h_d = 0.0001 m) are bonded over the ABH region from x_{d1} = 0.07 m to x_{d2} = 0.09 m. Note the model considers the full coupling of the layers, albeit very thin, with the host beam. For the energy transmission study, however, analysis is only focused on the part related to the host beam, although the energy flows into the damping layer part is also inherently calculated. Plotted in Fig. 12 is the comparison of the input power flow of the ABH beam with and without damping layers. It can be observed that the introduction of the damping layers causes a significant attenuation of power input amplitude at various modal frequencies, but a general increase at other frequencies. The underlying reason for this phenomenon is attributed to the fact that damping exerts different effects on the final balance between the two contributors to the total input power: the amplitude and the corresponding phase angle of the vibration response. At resonances, damping attenuates the vibration response significantly with little effect on the phase anlge, thus leading to a reduction of the total input power. At non-resonant frequencies, however, an increase of the system damping does not affect the amplitude of vibration response much, but generates an obvious increase in the phase anlge contribution to the input power.

Presented in Fig. 13 is the structural intensity distribution of the ABH beam with damping layers at the same three frequencies investigated before, with results denoted by a black square. For comparison purpose, the results of the ABH beam without damping layers shown in Fig. 9 are also given here again, marked as a red circle. For convenience, different regions of
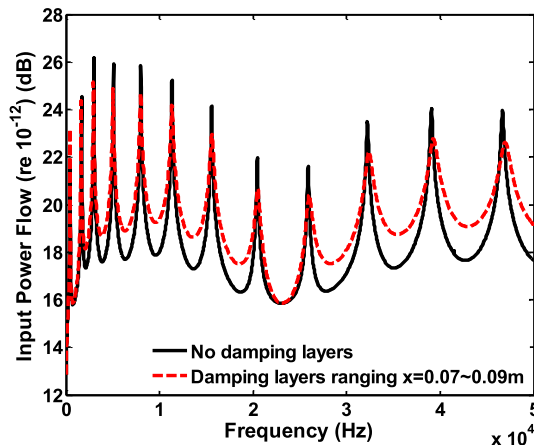

Fig. 12. Comparison of input power flow frequency response of ABH beam structure with and without damping layers.
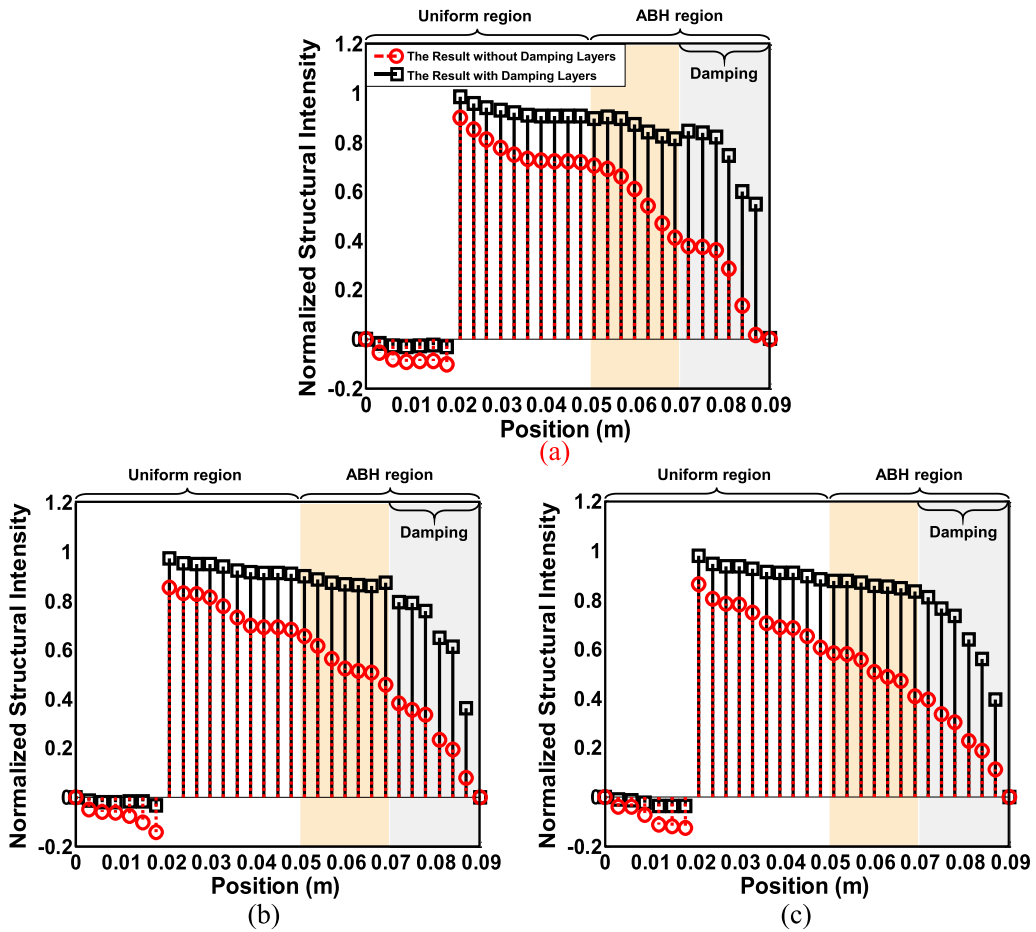
Fig. 13. Influence of damping layers on the normalized structural intensity distributions of ABH beam under excitation frequencies: (a) 5072 Hz; (b) 15564 Hz; (c) 39070 Hz.
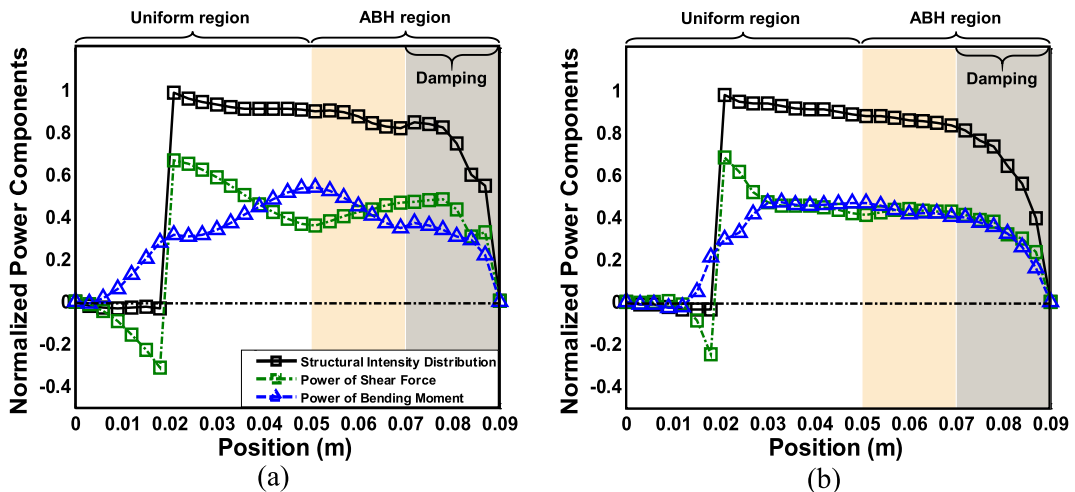

Fig. 14. Normalized power components due to the shear force and bending moment at two representative frequencies of ABH beam with damping layers: (a) 5072 Hz; (b) 39070 Hz.

the beams are marked as shadowed areas of different colors. Generally speaking, a relatively flat structural intensity distribution is observed within the uniform portion of the beam (on both sides of the excitation point), suggesting a relatively weak energy dissipation inside the structure. The trend persists until the entrance of the coating area, starting from which a sudden and rapid decrease is produced, testifying an accentuated energy dissipation within this area. At 5072 Hz, fluctuations associated with the structural intensity variation can be observed. When frequency increases, the overall trends become more uniform and smoother. Different from the energy dissipation effect of structural damping shown in Fig. 9, the application of the damping layers significantly enhances the ABH effect by making the tip region an energy sink, evidenced by the gradient variation of structural intensity distribution within the ABH area.

Structural intensity analysis associated with the shear force and bending moment components is also revisited in the presence of damping layers, and the calculated results are presented in Fig. 14. It can be seen that the general pattern is similar to that of the ABH beam without damping layers, while a significant decrease in the power levels mainly occurs in the damping layer region. At a much higher excitation frequency, vibrational energy transmission related with shear force and the bending moment components are almost equal to each other in the region away from point force, each taking roughly 50%. This is another testimony of the ABH effect in the sense that the damping layers enhance the energy sink phenomenon, producing a quasi-perfect anechoic termination with behaviors analogues to an infinite beam.

4. Conclusions

In this paper, a revamped semi-analytical model for power flow and structural intensity analysis of an elastically restrained Euler-Bernoulli ABH beam is established. An energy formulation is employed for the dynamic description of a beam structure with arbitrary thickness variation profile, expanded into a general Fourier series representation. Under Rayleigh-Ritz framework, admissible functions which ensure sufficient smoothness of the displacement functions in the entire solving domain are developed using an improved Fourier series expansion with boundary auxiliary trigonometric terms. Owing to the spatial derivative property of the decomposition series, internal force/moment terms required for the power flow and structural intensity calculations can be achieved through a term-by-term differential operation.

Numerical examples are presented to validate the proposed model through comparisons with exact solutions and Finite Element results using both uniform and ABH beams. Results show that high-order modal parameters can be accurately predicted, and a rapid convergence can be achieved in both free and forced vibration analyses. For the determination of the internal forces leading to the structural intensity, in which up to third order derivative terms of the structural displacement are involved, a suitable truncation of the decomposition can guarantee the accuracy of the power flow calculation. Using the model, power flow and structural intensity analyses on ABH beams without and with damping layers are carried out, leading to the following main conclusions.

(1) For the bare ABH beam without damping layer, vibrational energy, as characterized by the structural intensity distribution, diverges from the excitation position to the ABH region with fluctuations. Its spatial gradient, characterizing the local energy dissipation, shows obvious position-dependent characteristics. With the increase of the frequency, the gradient of the structural intensity distribution becomes more uniform, suggesting that the energy dissipation takes place across the entire beam due to the structural damping, with observable yet limited ABH effect at the tip area.

(2) With the damping layers covering the tip part of the ABH beam, ABH shows its effect in multiple aspects. First, a global increase in the normalized structural intensity is observed as compared with its counterpart without damping layers. Second, the structural intensity distribution shows rather uniform distribution before the coated area, after which a sudden and drastic decrease is observed, more obviously when frequency increases. Both observations confirm the fact that the presence of the damping layers enhances the ABH effect in making the tip area as an energy sink.

(3) Energy components associated with the internal shear force and the bending moment in the ABH beam commute to each other and gradually take equal part when approaching the ABH tip and when frequency increases. This phenomenon becomes more obvious with the addition of the damping layers in ABH region, making the ABH tip a quasi-anechoic termination with behaviors analogues to an infinite beam.

This work establishes a semi-analytical model for the power flow analyses of elastically restrained ABH beams for the first time, which can be used for energy transmission mechanism study and further optimal design of ABH beam structures. The special feature of the model in dealing with arbitrary thickness variation of the beam will further be exploited to maximize the ABH-specific effects in future applications.

Acknowledgement

Appendix

Formulas for **M**, **K**, and **F**:

$$M = M_{beam} + M_{damp}$$

$$K = K_{beam} + K_{damp}$$

$$i = 1\tilde{5}, \ j = 2\tilde{5}, \ s = m+1, \ t = \begin{cases} m'+1, i=1 \\ 1, i \neq 1 \end{cases}, \ m = m' = 0 \sim \infty$$

For the beam part, the **M** and **K** matrices are expressed as follows. When it comes to the damping layer part, the **M** and **K** matrices are similar, via making the upper and lower limits of the integral as $xd2$ and $xd1$, instead of L and 0 and using material parameters of the damping layers accordingly.

$$\{M_{1-i}\}_{s,t} = \begin{cases} \sum_{n=0}^{\infty} \alpha_n \rho \omega^2 \int_0^L \cos(\lambda_{Ln}x)\cos(\lambda_{Lm}x)\cos(\lambda_{a_1 m'}x)dx, i=1 \\ \sum_{n=0}^{\infty} \alpha_n \rho \omega^2 \int_0^L \cos(\lambda_{Ln}x)\cos(\lambda_{Lm}x)\zeta_{(i-1)L}(x)dx, i \neq 1 \end{cases}$$

$$\{M_{j-i}\}_{1,t} = \begin{cases} \sum_{n=0}^{\infty} \alpha_n \rho \omega^2 \int_0^L \cos(\lambda_{Ln}x)\zeta_{(j-1)L}(x)\cos(\lambda_{Lm'}x)dx, i=1 \\ \sum_{n=0}^{\infty} \alpha_n \rho \omega^2 \int_0^L \cos(\lambda_{Ln}x)\zeta_{(j-1)L}(x)\zeta_{(i-1)L}(x)dx, i \neq 1 \end{cases}$$

$$\{K_{1-i}\}_{s,t} = \begin{cases} \begin{bmatrix} \sum_{n=0}^{\infty} \beta_n E \lambda_{Lm}^2 \lambda_{Lm'}^2 \int_0^L \cos(\lambda_{Ln}x)\cos(\lambda_{Lm}x)\cos(\lambda_{Lm'}x)dx \\ + \lambda_{Lm}\lambda_{Lm'}\sin(\lambda_{Lm}0)\sin(\lambda_{Lm'}0)K_{b0}|_{x=0} + \cos(\lambda_{a_1 m}0)\cos(\lambda_{a_1 m'}0)k_{b0}|_{x=0} \\ + \lambda_{Lm}\lambda_{Lm'}\sin(\lambda_{Lm}L)\sin(\lambda_{Lm'}L)K_{b1}|_{x=L} + \cos(\lambda_{Lm}L)\cos(\lambda_{Lm'}L)k_{b1}|_{x=L} \end{bmatrix}, i=1 \\ \begin{bmatrix} \sum_{n=0}^{\infty} -\beta_n E \lambda_{Lm}^2 \int_0^L \cos(\lambda_{Ln}x)\cos(\lambda_{Lm}x)\zeta_{(i-1)L}''(x)dx \\ -\lambda_{Lm}\sin(\lambda_{Lm}0)\zeta_{(i-1)L}'(0)K_{b0}\big|_{x=0} + \cos(\lambda_{Lm}0)\zeta_{(i-1)L}(0)k_{b0}|_{x=0} \\ -\lambda_{Lm}\sin(\lambda_{Lm}L)\zeta_{(i-1)L}'(L)K_{b1}\big|_{x=L} + \cos(\lambda_{Lm}L)\zeta_{(i-1)L}(a_1)k_{b1}|_{x=L} \end{bmatrix}, i \neq 1 \end{cases}$$

$$\{K_{j-i}\}_{1,t} = \begin{cases} \begin{bmatrix} \sum_{n=0}^{\infty} -\beta_n \lambda_{Lm'}^2 E \int_0^L \cos(\lambda_{Ln}x)\zeta_{(j-1)L}''(x)\cos(\lambda_{Lm'}x)dx \\ -\lambda_{Lm'}\zeta_{(j-1)L}'(0)\sin(\lambda_{Lm'}0)K_{b0}\big|_{x=0} + \zeta_{(j-1)L}(0)\cos(\lambda_{Lm'}0)k_{b0}|_{x=0} \\ -\lambda_{Lm'}\zeta_{(j-1)L}'(L)\sin(\lambda_{Lm'}L)K_{b1}\big|_{x=L} + \zeta_{(j-1)L}(a_1)\cos(\lambda_{Lm'}L)k_{b1}|_{x=L} \end{bmatrix}, i=1 \\ \begin{bmatrix} \sum_{n=0}^{\infty} \beta_n E \int_0^L \cos(\lambda_{Ln}x)\zeta_{(j-1)L}''(x)\zeta_{1L}''(x)dx \\ + \zeta_{(j-1)L}'(0)\zeta_{(i-1)L}'(0)K_{b0}\big|_{x=0} + \zeta_{(j-1)L}(0)\zeta_{(i-1)L}(0)k_{b0}|_{x=0} \\ + \zeta_{(j-1)L}'(L)\zeta_{(i-1)L}'(L)K_{b1}\big|_{x=L} + \zeta_{(j-1)L}(a_1)\zeta_{(i-1)L}(L)k_{b1}|_{x=L} \end{bmatrix}, i \neq 1 \end{cases}$$

$$\{F_{1-1}\}_{s,1} = F\cos(\lambda_{Lm}x_f)$$

$$\{F_{j-1}\}_{1,1} = F\zeta_{(j-1)L}(x_f)$$

References

[1] V. Kralovic, V.V. Krylov, Damping of flexural vibrations in tapered rods of power-law profile: experimental studies, Inst. Acoust. 29 (5) (2007) 66–73.
[2] E.P. Bowyer, V.V. Krylov, Damping of flexural vibrations in turbofan blades using the acoustic black hole effect, Appl. Acoust. 76 (1) (2014) 359–365.
[3] J. Deng, L. Zheng, P.Y. Zeng, Y.F. Zuo, O. Guasch, Passive constrained viscoelastic layers to improve the efficiency of truncated acoustic black holes in beams, Mech. Syst. Sig. Process. 118 (2019) 461–476.
[4] L. Zhao, S.C. Conlon, F. Semperlotti, Broadband energy harvesting using acoustic black hole structural tailoring, Smart Mater. Struct. 23 (6) (2014) 065021-1-9.
[5] L. Zhao, S.C. Conlon, F. Semperlotti, An experimental study of vibration based energy harvesting in dynamically tailored structures with embedded acoustic black holes, Smart Mater. Struct. 24 (6) (2015) 065039-1-9.
[6] S.C. Conlon, J.B. Fahnline, F. Semperlotti, P.A. Feurtado, Enhancing the low frequency vibration reduction performance of plates with embedded Acoustic Black Holes, The 43rd International Congress on Noise Control Engineering, Melbourne, 2014.
[7] L.L. Tang, L. Cheng, Broadband locally resonant band gaps in periodic beam structures with embedded acoustic black holes, J. Appl. Phys. 121 (19) (2017) 194901-1-9.
[8] M.A. Mironov, Propagation of a flexure wave in a plate whose thickness decreases smoothly to zero in a finite interval, Sov. Phys. Acoust. 34 (3) (1988) 318–319.
[9] V.V. Krylov, Conditions for validity of the geometrical-acoustics approximation in application to waves in an acute-angle solid wedge, Sov. Phys. Acoust. 35 (2) (1989) 176–180.

[10] V.V. Krylov, Geometrical-acoustics approach to the description of localized vibrational modes of an elastic solid wedge, Am. Inst. Phys. 25 (1990) 137–140.

[11] V.V. Krylov, Localized acoustic modes of a quadratically-shaped solid wedge, Mosc. Univ. Phys. Bull. 45 (6) (1990) 65–69.

[12] V.V. Krylov, Propagation of localized vibration modes along edges of immersed wedge-like structures: geometrical-acoustics approach, J. Comput. Acoust. 7 (1) (1999) 59–70.

[13] V.V. Krylov, F.J.B.S. Tilman, Acoustic 'black holes' for flexural waves as effective vibration dampers, J. Sound Vib. 274 (3) (2004) 605–619.

[14] V.V. Krylov, New type of vibration dampers utilising the effect of acoustic 'black holes', Acta Acustica United with Acustica 90 (5) (2004) 830–837.

[15] L.L. Tang, L. Cheng, H.L. Ji, J.H. Qiu, Characterization of acoustic black hole effect using a one-dimensional fully-coupled and wavelet-decomposed semi-analytical model, J. Sound Vib. 374 (2016) 172–184.

[16] D.J. O'Boy, V.V. Krylov, Damping of flexural vibrations in circular plates with tapered central holes, J. Sound Vib. 330 (10) (2011) 2220–2236.

[17] D.J. O'Boy, E.P. Bowyer, V.V. Krylov, Point mobility of a cylindrical plate incorporating a tapered hole of power-law profile, Acoust. Soc. Am. J. 129 (6) (2011) 3475–3482.

[18] V.B. Georgiev, J. Cuenca, M.A.M. Bermudez, F. Gautier, L. Simon. Recent progress in vibration reduction using Acoustic Black Hole effect. 10ème Congrès Français d'Acoustique. Lyon, 12-16 Avril, 2010.

[19] V.B. Georgiev, J. Cuenca, F. Gautier, L. Simon, V.V. Krylov, Damping of structural vibrations in beams and elliptical plates using the acoustic black hole effect, J. Sound Vib. 330 (11) (2011) 2497–2508.

[20] E.P. Bowyer, D.J. O'Boy, V.V. Krylov. Damping of flexural vibrations in plates containing ensembles of tapered indentations of power-law profile. 164th Meeting of the Acoustical Society of America. Kansas. 22-26 October, 2012.

[21] V. Denis, F. Gautier, A. Pelat, J. Poittevin, Measurement and modelling of the reflection coefficient of an Acoustic Black Hole termination, J. Sound Vib. 349 (2015) 67–79.

[22] L.L. Tang, L. Cheng, Enhanced Acoustic Black Hole effect in beams with a modified thickness profile and extended platform, J. Sound Vib. 391 (2017) 116–126.

[23] S.C. Conlon, P.A. Feurtado, Progressive phase trends in plates with embedded acoustic black holes, J. Acoust. Soc. Am. 143 (2018) 921–930.

[24] H.L. Ji, J. Luo, J.H. Qiu, L. Cheng, Investigations on flexural wave propagation and attenuation in a modified one-dimensional acoustic black hole using a laser excitation technique, Mech. Syst. Sig. Process. 104 (2018) 19–35.

[25] W. Huang, H.L. Ji, J.H. Qiu, L. Cheng, Analysis of ray trajectories of flexural waves propagating over generalized acoustic black hole indentations, J. Sound Vib. 417 (2018) 216–226.

[26] D.U. Noiseux, Measurement of Power Flow in Uniform Beams and Plates, J. Acoust. Soc. Am. 47 (1970) 238–247.

[27] J. Pan, C.H. Hansen, Active control of total vibratory power flow in a beam. I: physical system analysis, J. Acoust. Soc. Am. 89 (1991) 200–209.

[28] T.Y. Li, W.H. Zhang, T.G. Liu, Vibrational power flow analysis of damaged beam structures, J. Sound Vib. 242 (1) (2001) 59–68.

[29] A. Carcaterra, A. Sestieri, Energy density equations and power flow in structures, J. Sound Vib. 188 (2) (1995) 269–282.

[30] G. Pavic, The role of damping on energy and power in vibrating systems, J. Sound Vib. 281 (2005) 45–71.

[31] G. Pavic, Vibration damping, energy and energy flow in rods and beams: governing formulae and semi-infinite systems, J. Sound Vib. 291 (2006) 932–962.

[32] X.Q. Wang, W.O. Wong, L. Cheng, Modal power flow with application to damage detection, Int. J. Eng. Sci. 47 (2009) 512–523.

[33] D.S. Cho, T.M. Choi, J.H. Kim, N. Vladimir, Structural intensity analysis of stepped thickness rectangular plates utilizing the finite element method, Thin-walled Struct. 109 (2016) 1–12.

[34] G. Petrone, M.D. Vendittis, S.D. Rosa, F. Franco, Numerical and experimental investigations on structural intensity in plates, Compos. Struct. 140 (2016) 94–105.

[35] H.A. Ba'ba'a, M. Nouh, An investigation of vibrational power flow in one-dimensional dissipative phononic structures, J. Vibr. Acoust. 139 (2) (2017), 021003-1-10.

[36] W. Huang, H.L. Ji, J.H. Qiu, L. Cheng, Wave energy focalization in a plate with imperfect two-dimensional acoustic black hole indentation, J. Vib. Acoust. 138 (6) (2016), 061004-1-12.

[37] L. Ma, S. Zhang, L. Cheng, A 2D Daubechies wavelet model on the vibration of rectangular plates containing strip indentations with a parabolic thickness profile, J. Sound Vib. 429 (2018) 130–146.

[38] J.T. Du, W.L. Li, G.Y. Jin, T.J. Yang, Z.G. Liu, An analytical method for the in-plane vibration analysis of rectangular plates with elastically restrained edges, J. Sound Vib. 306 (2007) 908–927.

[39] W.L. Li, X.F. Zhang, J.T. Du, Z.G. Liu, An exact series solution for the transverse vibration of rectangular plates with general elastic boundary supports, J. Sound Vib. 321 (2009) 254–269.

[40] J.T. Du, W.L. Li, Z.G. Liu, T.J. Yang, G.Y. Jin, Free vibration of two elastically coupled rectangular plates with uniform elastic boundary restraints, J. Sound Vib. 330 (2011) 788–804.

[41] L.L. Tang, L. Cheng, Loss of acoustic black hole effect in a structure of finite size, Appl. Phys. Lett. 109 (1) (2016) 014102-1-4.